CO Adsorption on Pt Nanoparticles in Low E-fields Studied by ATR-IR Spectroscopy in a Microreactor

A. Susarrey-Arce[*, 1, 2, 3], *R. M. Tiggelaar* [1], *J. G. E. Gardeniers* [1], *A. van Houselt* [2] *and L. Lefferts*[*, 2]

[1]Mesoscale Chemical Systems, and [2]Catalytic Processes and Materials, MESA+ Institute for Nanotechnology, University of Twente, P.O. Box 217, 7500AE Enschede, The Netherlands

[3]Open Innovation Hub for Antimicrobial Surfaces at the Surface Science Research Centre and Department of Chemistry, University of Liverpool, Oxford Street, UK L69 3BX, Liverpool

Corresponding Author

Dr. A. Susarrey-Arce, Phone: +44 1517 943 884, e-mail: A.Susarrey-Arce@liverpool.ac.uk

Prof. L. Lefferts, Phone: +31-53-489-2858, e-mail: l.lefferts@utwente.nl

Abstract

The adsorption of carbon monoxide (CO) on platinum (Pt) nanoparticles under influence of a low electrical field (E-field) is studied. The adsorption of CO is monitored by attenuated total reflection infrared (ATR-IR) spectroscopy, while an external electrical field is applied over the microreactor. Linearly (on top; CO_L), bridged (2 fold hollow; CO_B) and multiply (3 fold hollow; CO_{MB}) adsorbed CO species were found on the Pt nanoparticles. In a sequence of adsorption experiments the integrated ATR-IR intensity of the absorption band of the linearly adsorbed CO_L was found to reach steady state values after an initial decrease, which is attributed to a loss of Pt surface area due to sintering of the Pt metal nanoparticles. The application of electrical fields result in changes in the ratio between linearly adsorbed CO, on top of Pt, versus CO adsorbed on multiple Pt atoms.

Keywords: ATR-IR, CO adsorption, E-field, Microreactor, Infrared

1. Introduction

CO adsorption on group VIII metal catalysts has been intensively studied over the years, because of the relevance of CO as a probe of the available amount of adsorption sites on surfaces of catalysts. CO is also important in the catalytic conversion for pollution control[1, 2] and often used as model reactant for commercially industrial processes, including naphtha reforming, (de)hydrogenation, and oxidation reactions[3, 4]. The electronic properties of the metal catalyst surface play a vital role in the reactivity. The charge on the surface of the catalyst is generally influencing the adsorption and reactivity of CO[5]. Baker and coworkers demonstrated nicely, using a solid-state charge-based microreactor, that a negative charge on the surface of the Pt catalyst increases the activity for CO oxidation, while a positive charge decreases the activity for CO oxidation[6]. Effects of the work function of the metal catalyst on the reaction rate are reported by Vayenas and co-workers[7-9]. H. J. Kreuzer reported calculations of the adsorption of chemical species on metal surfaces[10] in the presence of weak electrical fields, where at fields below ~$1x10^8$ V/cm atoms and molecules polarize, leading to drastic changes in the adsorption properties of molecules on surfaces. This is due to the distortion of the binding orbital, which leads to new bonding properties[10].

Here we present a study on the influence of a weak electric field on the adsorption of CO in a home-built microreactor. In order to generate the required field strengths we fabricated microstructures similar to field emitter tips. The sharp curvature of the microstructures integrated in the gas flow channel of the microreactor enhances the local E-field. CO is used as a probe molecule for our newly developed microreactor, in which we are able to vary an external E-field over the microreactor and simultaneously monitor the catalyst interface with Attenuated Total Reflection (ATR) infrared (IR) spectroscopy.

2. Experimental section

2.1 Fabrication of the ATR-IR microreactors

The main device used in this study is a microreactor designed for simultaneous application of an external (E-field) and *in situ* ATR-IR. A schematic representation of the microreactor is shown in **Figure 1(a)**. Details of the fabrication and choices of the materials for this microreactor have been described elsewhere[11-15]. In brief, the E-field is applied via Cu/$TiSi_2$ contacts (Cu/green bars in **Figure 1(a)**) to the top and bottom electrode. The bottom electrode, fabricated from a double side polished *p*-type (500 μm thickness, 5-10 Ωcm resistivity, Okmetic Finland) Si(001) wafer, acts as total internal reflection element for the ATR-IR measurements. On the top electrode, fabricated from a double side polished *p*+-type silicon (500 μm thickness, 0.01-0.02 Ωcm resistivity, Okmetic Finland), cylindrical pillars are micromachined. The interspace between the top of the micropillars and the ATR-IRE surface is ~ 2 μm. The width and length of the channel are 1.8 and 4.4 cm, respectively, leading to a total microreactor volume V of ~1.3 x 10^{-2} cm^3. The SiO_2 layer terminating the ATR-IRE crystal (colored in orange in **Figure 1**(**a**)) is defined by dipping the ATR-IRE containing wafer in 1% HF for about 25 min (after photolithography and prior to thermal bonding), during which the initial ~ 2 μm SiO_2 layer is locally thinned down to 140 nm ± 40 nm.

2.2 Coating of the gas flow channel with Pt nanoparticles

Commercially available Pt nanopowder from Sigma-Aldrich (with an average particle size < 50 nm) was suspended as received in *n*-hexane (Sigma Aldrich, > 99.00% purity over molecular sieve). The Pt nanoparticle suspension was prepared by adding 50 mg Pt nanopowder to 1 mL of *n*-hexane (which would be enough to fully cover the entire bottom electrode with a ~ 50 nm layer of Pt particles), followed by vigorous ultra-sonication for 3 h. The microreactor was coated three times subsequently by flowing the 50 mg/mL Pt nanoparticles in *n*-hexane suspension through the microreactor flow channel, and dried overnight under 10% oxygen/helium (O_2/He) mixture

(99.999% purity from Praxair) with a flow of ~30 μL/min (with a mass flow controller of Brooks, model 5850/BC).

2.3 Electrical characterization of the Pt coated microreactors

Subsequent to the coating with Pt nanoparticles the electrical response of the microreactors was investigated. A Keithley 2410 power supply programmed via a home-written Labview script was used to apply the voltage pulses and to record the electrical response in the form of I(V) curves.

2.4 Pre-treatment of the microreactors

A pre-treatment to remove any trace of *n*-hexane from the deposition process and to reach a stable IR signal was performed prior to ATR-IR microreactor experiments, consisting of four cycles of CO chemisorption and subsequent CO oxidation with total flows of 30 μL/min of CO (99.97% purity) and premixed 10% O_2/He mixture (99.999% purity), respectively (all gases from Praxair). During these pre-treatment cycles, no E-field was applied to the microreactor. After these pre-treatment cycles, 30 μL/min of hydrogen (99.99% pure H_2 from Praxair) was flown through the microreactor for 1 h. Gas flows (i.e. single composition and from premixed compressed gas cylinders) were controlled with mass flow controllers from Brooks (model 5850/BC). All experiments are performed at room temperature.

2.5 CO adsorption/oxidation cycles

CO (99.97% purity, Praxair) was flowed (30 μL/min) for 210 minutes followed by a premixed 10% v/v O_2/He (99.999% purity, Praxair) mixture (30 μL/min) for 360 min to remove the adsorbed CO, thereby preparing the surface of the Pt nanoparticles for the next CO adsorption experiment. These experiments (CO adsorption and subsequent oxidation), hereafter termed as an "adsorption cycle", were performed during the application of respectively ± 5 V, ± 15 V and ± 25 V over the microreactor in subsequent experiments, keeping the top electrode connected to earth as indicated in **Figure 1(a)**. To verify the influence of the external E-field over the deposited Pt catalyst, a "reference

experiment" without E-field was performed between every two adsorption cycles with a flow rate of 30 μL/min.

2.6 ATR-IR measurements

During each experiment *in situ* ATR measurements were carried out in a Fourier Transform Infrared (FT-IR) spectrometer, Tensor 27 (Bruker Optics) with a MCT D316/6-L detector cooled with liquid N_2 and a resolution of 8 cm^{-1} & 256 co-added scans. The microreactor was positioned in a home-designed ATR cell[12], which consists of four concave polished mirrors mounted on a metal holder with electrical connectors. ATR-IR spectra are measured against a background in He, and are shown baseline corrected.

3. Results

3.1 Coating the gas flow channel of the ATR-IR microreactor with Pt particles

A representative Scanning Electron Microscope (SEM) image of the deposited Pt nanoparticles on the ATR-side (bottom electrode in **Figure 1(a)**) after fracturing a freshly coated ATR-IR microreactor into small pieces with a diamond dresser is shown in **Figure 1(b)**. The inset shows an image of the deposited Pt nanoparticles at higher magnification. **Figure 1(c)** shows a SEM image after coating a diced, flat Si substrate with the Pt nanoparticles, following a procedure similar to the one described in the experimental section 2.2. **Figure 1(d)** shows a SEM image of the Pt nanoparticles in a manually cleaved microreactor after 20 E-field CO adsorption/oxidation cycles. Energy dispersive X-rays spectroscopy reveals a Pt coverage of ~ 0.14 $\mu g/mm^2$ (assuming a penetration depth of ~ 5 μm for the electron beam used in EDX).

The images in **Figures 1(b)-(d)** show Pt particles on the bottom-electrodes (confirmed by the SEM image of the backscattered electrons, EDX spectroscopy, and X-ray photo-electron spectroscopy, XPS, not shown) with a bimodal size distribution. Large particles with diameters of 100 to 150 nm are observed, as well as small particles with diameters around 10 nanometers. Moreover,

smaller Pt particles of diameter < 10 nm are also observed in **Figures 1(b)-(c),** while in **Figure 1(d)** these smaller Pt particles are less frequently observed. In addition, in **Figure 1(d)** the coalescence of Pt particles shows up as neck-formation between two adjacent particles (see open yellow ellipse). For the top electrodes with pillars, similar coalescence was observed.

3.2 Electrical characterization of the microreactors

I(V) curves are recorded for the Pt nanoparticle-coated microreactor with a premixed 10% O_2/He mixture flow through the microreactor. The results are plotted as Fowler-Nordheim graphs, i.e. $\ln(J/E^2)$ *vs.* $1/E$[11, 12, 16], in **Figures 1(e)** and **1(f)**. **Figure 1(e)** is measured with the E-field directed downwards (from the top electrode with the pillars towards the bottom ATR-IRE electrode), while **Figure 1(f)** is measured with the E-field directed upwards. The current density in **Figure 1(e)** was calculated using only the total area of the flat micropillar top surfaces (~0.4 cm^2), *i.e.* the surface area where the gap between top and bottom electrode is 2 μm[11, 12]. The total geometric surface area of the ATR-IRE flat electrode in **Figure 1**(**f**) was 7.9 cm^2.

3.3 CO adsorption ATR-IR measurements

Pre-treatment results.

ATR-IR measurements during a single pre-treatment cycle (no applied E-field) of the microreactor are shown in **Figure 2(a).** Infrared absorption peaks develop during adsorption at initially 2068 cm^{-1}, shifting to 2050 cm^{-1} with increasing surface coverage at 1840 cm^{-1} and multiple bands are observed from 1730 to 1620 cm^{-1}, with a maximum at 1708 cm^{-1}. The absorption band initially observed at 2068 cm^{-1}, which shifts to 2050 cm^{-1} with increasing surface coverage can be assigned to linearly adsorbed CO (hereafter referred to as CO_L). The absorption band at 1840 cm^{-1} can be assigned to bridging CO (CO_B) and the bands around 1708 cm^{-1} are ascribed to a combination of multiply adsorbed CO (CO_{MB}). The weak maximum at 1656 cm^{-1} is attributed to the presence of water in the CO feed and is corrected for in the inset of **Figure 2(a)**.

The ATR-IR spectra in **Figure 2(b)** were collected after 210 min, at the end of each of the CO adsorption steps during the pre-treatment cycles (in absence of any E-field). Note the decrease in the intensity of the CO absorption bands after the subsequent pre-treatment cycles.

CO adsorption/oxidation cycles in a weak external E-field

Integrated intensities (after correction for the presence of water in the CO feed) of the CO absorption bands in *subsequent* adsorption cycles are displayed in **Figure 3**. The integration boundaries for all the CO_L, CO_B and CO_{MB} are 2110 – 1900, 1900 – 1750 and 1750 – 1600 cm^{-1}, respectively. The integrated intensity is shown from t = 0, the moment that the CO flow through the microreactor is started, over a time lapse of 200 minutes. **Figures 3(a)**, **(3c)** and **3(e)** show the integrated intensities of the CO_L, CO_B and CO_{MB} absorption bands, respectively, in a subsequent set of adsorption cycles for increasing values of an E-field applied in the *downwards* direction, while **Figures 3(b)**, **(3d)** and **3(f)** show the integrated intensities of the CO_L, CO_B and CO_{MB} absorption bands, respectively, in a subsequent set of adsorption cycles for increasing values of an E-field applied in the *upwards* direction. In **Figure 3(a)** and **3(b)** the integrated intensity starts to rapidly increase after a few minutes and levels off to a constant value after ~80 minutes. This constant value is higher in the first two experiments (with applied voltages 0 and – 5 V) in **Figure 3(a)** and has similar values for the other experiments in **Figures 3(a)** and **3(b)**, *i.e.* at ~ 0.6 of the *y*-axes for the total integrated area of CO_L. Two reference measurements (*i.e.* without E-field, see experimental section 2.5) are performed prior to the application of V = -15 and V = -25 in **Figure 3(a)**, see 0V (-15) and 0V (-25). Note that a reduction pre-treatment with H_2 was carried out between the experiment resulting in **Figure 2(b)** and the experiments shown in **Figure 3** (see experimental section 2.4). No changes in the ATR-IR spectra were found during these reduction experiments.

The signal-to-noise ratio in **Figures 3(c)-(f)** is much lower, due to the lower peak intensities of the CO_B and CO_{MB} absorption bands. In **Figures 3(c)-(f)** the integrated intensities start to increase immediately from t = 0 and seem to level off to a constant value around t = 100 min. Note that in the

experiment with 25 V applied over the microreactor the increase in the integrated intensity in **Figures 3(d)** and **(f)** is significantly larger than at lower potentials.

In between every CO adsorption cycle in which an E-field was applied an adsorption cycle without an applied E-field (*i.e.* 0 V) was performed as reference. ATR-IR absorption spectra at t = 200 min of these reference measurements are shown in **Figure 4**. The broad and strongly asymmetric CO_L absorption band has initially a maximum at 2052 cm^{-1} (after 0 cycles, only pretreated), which shifts to ~2080 cm^{-1} after 20 CO adsorption cycles, accompanied by a ~25% decrease of the integrated signal.

Figures 5(**a**) and **5**(**b**) present IR spectra including CO_B and CO_{MB} absorption bands measured (in between t =150 and 155 min) in presence of different E-fields in the downwards and upwards direction. In **Figure 6** we plotted the time averaged (from t = 150 to 210 min.) CO_L/CO_B and CO_L/CO_{MB} ratios of the integrated peak areas as a function of the applied potential (see **Figure 3**). For the applied negative potentials (0 to -25 V) the CO_L/CO_B and CO_L/CO_{MB} ratios decrease slightly with increasing field strength, while for positive potentials (0 to 25 V) a significant decrease in the CO_L/CO_B and CO_L/CO_{MB} ratios is observed with increasing field strength.

4. Discussion

4.1 Coating the gas flow channel of the ATR-IR microreactor with Pt particles

From the SEM image of the ATR-IRE of a fractured microreactor in **Figure 1(b)** it can be observed that the Pt nanoparticles are homogeneously distributed over the entire surface forming square clusters. This square distribution pattern, where each square has a width-of about 16±6 μm, can be attributed to the presence of the pillars with pitch (*i.e.* pillar diameter + pillar-to-pillar interspace) dimensions of 20 μm at a distance of only 2 μm on the opposite top electrode during the drying process of the Pt suspension in *n*-hexane, as a consequence of which capillary forces act during the drying process. The successful deposition of Pt nanoparticles with *n*-hexane as a solvent in the

microreactor is related to its low surface tension, since similar Pt functionalization experiments with water or ethanol as solvent within the microreactor failed.

4.2 Electrical characterization of the microreactors

The Fowler-Nordheim (FN) plots in **Figures 1(e)** and **1(f)** reveal linear behavior at low 1/E values, which is indicative of E-field driven electron emission. The onset field strength for field emission can be extracted from the intercept with the 1/E axis in **Figures 1(e)** and **1(f)**. A higher 1/E value is needed to start electron emission from the flat surface in **Figure 1(e)** compared to electron emission from the micropillars in **Figure 1(f)**. The relatively sharp edges of the pillar tips locally enhance the E-field, leading therewith to a lower onset E-field value for electron emission from the pillared top electrode. From **Figures 1(e)** and **1(f)** the calculated onset values for electron emission correspond to application of ~ -4 V and ~ 1 V over the microreactor, respectively.

It is clear from FN plots that below E-field emission (*i.e.* < 1 and -4 V) the reactor surface becomes polarized and electron field emission does not yet occur at a significant rate. We have estimated that electron emission happens above 1 V and -4 V in the upward and downwards potentials. This emission is expected to occur within a small part of the microreactor, where the distance between the top of the micropillars and the ATR-IRE surface is the smallest, namely 2 μm.

4.3 CO adsorption ATR-IR measurements

In **Figures 2(a)** and **2(b)**, the assignments of the CO absorption peaks at 2068-2050 cm^{-1}, 1840 cm^{-1}, 1708 cm^{-1} to linear (CO_L), bridging (CO_B) and other multiply-bonded (CO_{MB}) CO, respectively, is in accordance with literature[17, 18]. The weak absorption at 1656 cm^{-1} (for which is corrected in the inset of **Figure 2(a)**) is most likely due to the presence of water[19, 20]. The exact structural assignment of the adsorption configuration for the 1708 cm^{-1} absorption band remains unclear, but likely candidates are a long 2-fold bridge (which could for instance occur between 2 adjacent ridges of the

missing row reconstructed (110) surface) or CO molecules σ-bonded to one Pt atom and σ or π bonded to a second one[17, 18].

An interpretation for the red-shift from 2065 cm^{-1} to 2050 cm^{-1} in **Figure 2**(**a**) needs further investigation as no clear conclusion can be drawn from the recorded IR measurements. An increase in dipole-dipole interaction strength would show up as a blue-shift in the spectra, which we would expect. The increasing dipole-dipole interaction is, however, apparently compensated by another effect in our measurements. A higher degree of back-donation to the π* CO orbitals would result in a red-shift. A possible reason for this higher degree of back donation could be co-adsorption of water, which is present as impurity in the CO feed as indicated by the absorption at 1656 cm^{-1}. Water adsorbs via the oxygen and is able to donate electrons to the Pt. As a consequence, the back-donation from Pt to CO increases, leading to a red-shift. Co-adsorbing water is indeed reported to cause a red-shift of ~20 cm^{-1} in the CO_L absorption peak[19, 20].

The successive ATR-IR measurements during CO adsorption in **Figure 2(b)** reveals a continuous decrease in the intensity of the CO_L band (see cycle 3 and cycle 4), followed by a further (~40%) drop in the total ATR-IR intensity in the subsequent experiments in **Figure 3** (compared to the initial intensity in **Figure 2**), most prominently visible in **Figure 3(a)** as a decrease in integrated intensities. More precisely, the decrease in integrated intensity is clearly observable in the first two adsorption cycles in **Figure 3(a)** (*ca.* 20% of the integrated signal). After these two cycles the integrated CO_L absorption intensity in **Figures 3(a)** and **3(b)** levels off around a value slightly above 0.6 (see, y axis-total integrated area). We assign this decrease in intensity in **Figures 2** and **3(a)** to a decrease in available adsorption sites during the experiments as a consequence of particle restructuring during CO and/or O_2 exposure. For the reference measurements 0V, 0V(-15) and 0V(-25) performed in between two E-field measurements (see **Figure 3(a)**) a similar decay is observed, supporting this particle restructuring during the CO/O_2 exposure. Furthermore, CO_L ATR-IR absorption spectra in **Figure 4** show significant changes between 0 and 20 cycles. The absorption maximum is blue-shifted from 2052 cm^{-1} in the first spectrum to 2080 cm^{-1}. A blue-shift for the CO_L absorption band for larger

Pt particles compared to smaller ones is well documented[21]. This shift is consistent with our ripening interpretation and in good agreement with the observed decrease in the total integrated signal in **Figures 2** and **3(a)**, which strongly suggests that this ripening mechanism leads to a lower surface area for CO adsorption. Indeed, clearly ripened particles are observed after 20 CO adsorption/oxidation cycles in **Figure 1d**. Besides ripening, the blue-shift of the CO_L peak in **Figure 4** could also be explained by partial oxidation of the Pt nanoparticles. CO adsorption on slightly oxidized Pt surface will result in a blue-shift of the CO_L IR band relative to CO adsorption on a clean Pt surface[21, 22]. Note that due to the lower signal-to-noise ratio in **Figures 3(c)** to **(f)** it is not possible to observe a similar decay in the integrated intensities after the first experiments.

Enhanced particle restructuring in CO and/or O_2 pressure was observed and documented before[24-31]. CO induced changes in the surface morphology of Pt nanoparticles are observed by infrared spectroscopy[24], scanning tunneling microscopy[25, 28, 31], environmental transmission electron microscopy[29], and grazing incidence small-angle X-ray scattering[27] and are attributed to an Ostwald ripening mechanism (migration of atoms)[25, 27, 28] or Smoluchowski ripening (particle migration)[28]. In Ref. 26 O_2 induced ripping of Pt nanoparticles is attributed to an Ostwald ripening process, while in Ref. 31 enhanced ripping is observed when both CO and O_2 are present. Whether in the present study the loss of surface area should be attributed to Ostwald ripening, Smoluwchowski ripening, or both[32], cannot be answered with the data at hand. The observed neck-formation (see **Figure 1(d)**) could originate from both processes individually and from a combination of the two ripening mechanisms.

For CO_B and CO_{MB}, an increase in the peak height is observed in **Figures 5(a)** and **5(b)** at 25 and – 25 V. The highest intensity growth is revealed in **Figure 5**(**b**) for an applied potential of 25 V along with a red-shift to 1700 cm^{-1} as the applied E-field increases. To assess possible CO dissociation effects caused by high applied electrical potentials, in **Figure SI-1** we compare the integrated CO_{MB} as a function of time at different electrical potentials. No changes in oxidation time are observed for -25 V, 25V and 0V, suggesting that similar amounts of CO species (CO_L, CO_B and CO_{MB}) are adsorbed on Pt nanoparticles. Therefore, possible dissociated CO might be minimal.

This shift is attributed to an increase in the bond strength due to a reduce π back donation when the electron density on the Pt lowered by the application of the electrical potential. Significant loss of surface area is endorsed to a loss of IR intensity during CO exposure cycles. The effects flatten off after V = - 5 (see **Figure 3**), and thus any change in the IR ration in **Figure 6** cannot be attributed to the loss of surface area, since the integrated values stayed constant after the measurement at - 5 V. Thus, changes in the CO_L/CO_B & CO_L/CO_{MB} ratios are assigned to the application of the E-field. These results indicate that the electronic modification of the platinum nanoparticles can be caused by the application of the electrical field, particularly at positive potentials, were a pronounced decrease in both ratios is observed. A change in the electronic structure of the (supported) metal particles influences the adsorption geometry of adsorbed CO[5, 20] as a consequence. Similar lowering of the CO_L/CO bridging ratios are observed (see **Figure 6**) for alkali-promoters during a catalytic chemical reaction, e.g. Pt/SiO_2[33] and Pt/Zeolites[34]. In these studies, the integrated intensity ratio of the CO_L/CO bridging drops significantly, suggesting an increase in the electron density on the metal atom with increasing alkalinity of the support[5, 18, 24, 33, 34]. Our results are in agreement with J. T. Miller *et al.*, who reported a shift to lower frequency and a decrease in the linear to bridging ratio as the alkalinity of the support increases[35]. For CO, a decrease in the binding energy of the Pt valence orbitals would result in a better overlap of the 5d–π∗ orbitals this leading to more π∗ electron density, a weaker C–O bond and a shift in the IR bands to lower energy. Likewise, their theoretical calculations predict a shift from linear to bridge-bonded CO when there is a better overlap of the 5d–π∗ orbitals. It is important to note that effects in the adsorption geometry of the molecule (*i.e.* increases of the CO_B and CO_{MB} integrated areas) due to an increase in temperature are unlikely. For such temperature effects a sharp drop (or increase) in the CO_B or CO_{MB} integrated area in **Figure 3** are expected at higher temperatures (~100° C)[18].

In short, by controlling the applied potentials to the ATR-IR microreactor, the adsorption geometry of CO_{MB} can be tuned. Therefore possible applications to increase selectivity during a catalytic chemical reaction can be expected.

5. Conclusions

We have studied the influence of the presence of low strength E-fields on CO adsorption on supported Pt particles *in situ* by ATR-IR in a sequence of CO adsorption/oxidation cycles. A decrease of the ATR-IR intensity of the CO_L absorption band is observed in subsequent CO adsorption/oxidation cycles. This observed decrease in the ATR-IR intensity is caused by a coarsening effect during the experiment and is not directly influenced by the direction or the magnitude of the applied E-field. Drops in the CO_L/CO_B and CO_L/CO_{MB} ratios are found. Excitingly, by combining ATR-IR spectroscopy with an E-field, new insights are generated regarding controlling the adsorption geometry of the tested adsorbate.

Acknowledgment

This work is financially supported by NWO (The Netherlands' Organization for Scientific Research) under grant No.700.58.041. The authors gratefully acknowledge K. Altena-Schildkamp, B. Geerdink, R. Lubkemann and S. Schlautmann for technical support.

References

(1) Berlowitz, P. J.; Peden, C. H. F.; Goodman, D. W. Kinetics of carbon monoxide oxidation on single-crystal palladium, platinum, and iridium *J. Phys. Chem.* **1988**, *92*, 5213-5221

(2) An, K.; Alayoglu, S.; Musselwhite, N.; Plamthottam, S.; Melaet, G.; Lindeman, A. E.; Somorjai, G. A. Enhanced CO oxidation rates at the interface of mesoporous oxides and Pt nanoparticles *J. Am. Chem. Soc.* **2013**, *135*, 16689-16696

(3) Jahel, A.; Avenier, P.; Lacombe, S.; Olivier-Fourcade, J.; Jumas, J.-C. Effect of indium in trimetallic Pt/Al_2O_3SnIn–Cl naphtha-reforming catalysts *J. Catal.* **2010**, *272*, 275-286

(4) Keresszegi, C.; Mallat, T.; Grunwaldt, J.-D.; Baiker, A. A simple discrimination of the promoter effect in alcohol oxidation and dehydrogenation over platinum and palladium *J. Catal.* **2004**, *225*, 138-146

(5) Mojet, B. L.; Miller, J. T.; Ramaker, D. E.; Koningsberger, D. C. A New model describing the metal–support interaction in noble metal catalysts *J. Catal.* **1999**, *186*, 373-386

(6) Baker, L. R.; Hervier, A.; Kennedy, G.; Somorjai, G. A. Solid-state charge-based device for control of catalytic carbon monoxide oxidation on platinum nanofilms Using External Bias and Light *Nano Lett.* **2012**, *12*, 2554-2558

(7) Vayenas, C. G.; Bebelis, S.; Neophytides, S. Non-faradaic electrochemical modification of catalytic activity *J. Phys. Chem.* **1988**, *92*, 5083-5085

(8) Vayenas, C. G.; Bebelis, S.; Ladas, S. Dependence of catalytic rates on catalyst work function *Nature* **1990**, *343*, 625-627

(9) Vayenas, C. G.; Bebelis, S.; Yentekakis, I. V.; Lintz, H.-G. Non-faradaic electrochemical modification of catalytic activity: a status report *Catal. Today* **1992**, *11*, 303-442

(10) Kreuzer, H. J. Physics and chemistry in high electric fields *Surf. Interface Anal.* **2004**, *36*, 372-379

(11) Susarrey-Arce, A.; Tiggelaar, R. M.; Sanders, R. G. P.; Geerdink, B.; Lefferts, L.; Gardeniers, J. G. E.; van Houselt, A. Temperature dependence of the 1727 cm^{-1} interstitial oxygen absorption band studied by attenuated total internal reflection infrared spectroscopy in a newly developed microreactor *J. Phys Chem C* **2013**, *117*, 21936-21942

(12) Susarrey-Arce, A.; Tiggelaar, R. M.; Morassutto M.; Geerlings, J.; Sanders, R. G. P.; Geerdink, B.; Schlautmann, S.; Lefferts, L.; van Houselt, A.; Gardeniers, J. G. E. A new ATR-IR microreactor to study electrical field driven processes, *Sens. Act. B* **2015**, *220*, 13-21

(13) Susarrey-Arce, A.; Marín, Á. G.; Nair, H.; Lefferts, L.; Gardeniers, J. G. E.; Lohse, D.; van Houselt, A. Absence of an evaporation-driven wetting transition on omniphobic surfaces *Soft Matter* **2012**, *8*, 9770-9770

(14) Susarrey-Arce, A.; Marín, Á. G.; Schlautmann, S.; Lefferts, L.; Gardeniers, J. G. E.; van Houselt, A. One-step sculpting of silicon microstructures from pillars to needles for water and oil repelling surfaces *Micromech. Microeng.* **2013**, *23*, 025004

(15) Tran, T.; Staat, H. J. J.; Susarrey-Arce, A.; Foertsch, T. C.; van Houselt, A.; Gardeniers, J. G. E.; Prosperetti, A.; Lohse, D.; Sun, C. Droplet impact on superheated micro-structured surfaces *Soft Matter*, **2013**, *9*, 3272- 3282

(16) Ravindra, N. M.; Zhao, J. Fowler-Nordheim tunneling in thin SiO_2 films *Smart Mater. Struct.* **1992**, *1*, 197-201

(17) De La Cruz, C.; Sheppard, N. An exploration of the surfaces of some Pt/SiO_2 catalysts using CO as an infrared spectroscopic probe *Spectrochimica Acta A* **1994**, *20*, 271-285

(18) Visser, T.; Nijhuis, T. A.; van der Eerden, A. M. J.; Jenken, K.; Ji, Y.; Bras, W.; Nikitenko, S.; Ikeda, Y.; Lepage, M.; Weckhuysen, B. Promotion effects in the oxidation of CO over zeolite-supported Pt nanoparticles *J. Phys. Chem. B* **2005**, *109*, 3822-3831

(19) Rupprechter, G.; Dellwig, T.; Unterhalt, H.; Freund, H.-J. High-pressure carbon monoxide adsorption on Pt(111) revisited: a sum frequency generation study *J. Phys. Chem B* **2001**, *105*, 3797- 3802

(20) Vaarkamp, M.; Mojet, B. L.; Kappers, M. J.; Miller, J. T.; Koningsberger, D. C. Hydrogen as a modifier of the structure and electronic properties of platinum in acidic zeolite LTL: a combined infrared and x-ray absorption spectroscopy study *J. Phys. Chem.* **1995**, *99*, 16067-16075

(21) Kweskin, S. J.; Rioux, R. M.; Habas, S. E.; Komvopoulos, K.; Yang, P.; Somorjai, G. A. Carbon monoxide adsorption and oxidation on monolayer films of cubic platinum nanoparticles investigated by infrared-visible sum frequency generation vibrational spectroscopy *J. Phys. Chem. B* **2006**, 110, 15920-15925

(22) Cant, N. W.; Donaldson, A. R.; Infrared spectral studies of reactions of carbon monoxide and oxygen on Pt/SiO_2 *J. Catal.* **1981**, 71, 320-330

(23) Allian, A. D.; Takanabe, K.; Fujdala, K. L.; Hao, X.; Truex, T. J.; Cai, J.; Buda, C.; Neurock, M.; Iglesia E. Chemisorption of CO and mechanism of CO oxidation on supported platinum nanoclusters *J. Am. Chem. Soc.* **2011**, *133*, 4498-4517

(24) Raskó, J. CO-induced surface structural changes of Pt on oxide-supported Pt catalysts studied by DRIFTS *J. Catal.* **2003**, *217*, 478-486

(25) Berkó, A.; Szökő, J.; Solymosi, F. Effect of CO on the morphology of Pt nanoparticles supported on TiO_2(1 1 0)-(1 × n) *Surf. Sci.* **2004**, *566*, 337-342

(26) Simonsen, S. B.; Chorkendorff, I.; Dahl, S.; Skoglundh, M.; Sehested, J.; Helveg, S. Ostwald ripening in a Pt/SiO_2 model catalyst studied by in situ TEM *J. Catal.* **2011**, *281*, 147-155

(27) Chaâbane, N.; Lazzari, R.; Jupille, J.; Renaud, G.; Soares, E. A. CO-induced scavenging of supported Pt nanoclusters: a GISAXS study *J. Phys. Chem. C* **2012**, *116*, 23362–23370

(28) Gerber, T.; Knudsen, J.; Feibelman, P. J.; Grana, E.; Stratmann, P.; Schulte, K.; Andersen, J. N.; Michely, T. CO-induced Smoluchowski ripening of Pt cluster arrays on the graphene/Ir(111) Moiré *ACS Nano* **2013**, *7*, 2020-2031

(29) Yoshida, H.; Matsuura, K.; Kuwauchi, Y.; Kohno, H.; Shimada, S.; Haruta, M.; Takeda, S. Temperature-dependent change in shape of platinum nanoparticles supported on CeO_2 during Catalytic reactions *Applied Physics Express* **2011**, *4*, 065001

(30) Hansen, P. L.; Wagner, J. B.; Helveg, S.; Rostrup-Nielsen, J. R.; Clausen, B. S.; Topsøe, H. Atom-resolved imaging of dynamic shape changes in supported copper nanocrystals *Science* **2002**, *295*, 2053-2055

(31) Bonanni, S.; Aït-Mansour, K.; Harbich, W.; Brune, H. Reaction-induced cluster ripening and initial size-dependent reaction rates for CO oxidation on $Pt_n/TiO_2(110)$-(1×1) *J. Am. Chem. Soc.* **2014**, *136*, 8702−8707

(32) Hansen, T. W.; Delariva, A. T.; Challa, S.R.; Datye, A. K.; Sintering of catalytic nanoparticles: particle migration or Ostwald ripening? *Accounts of Chemical research* **2013**, *46*, 1720–1730

(33) Koningsberger, D. C.; Ramaker, D. E.; Miller, J. T.; De Graaf, J.; Mojet, B. L. The direct influence of the support on the electronic structure of the active sites in supported metal catalysts: evidence from Pt-H anti-bonding shape resonance and Pt-CO FTIR data *Topic in Catal.* **2001**, *15*, 35-42

(34) Treesuko, P.; Srisuk, K.; Limtrakul, J.; Truong, T. N. Nature of the metal-support interaction in bifunctional catalytic Pt/H-ZSM-5 Zeolite *J. Phys. Chem. B* **2005**, *109*, 11940–11945

(35) Miller, J. T.; Mojet, B. L.; Ramaker, D. E.; Koningsberger, D. C.; A new model for the metal-support interaction evidence for a shift in the energy of the valence orbitals, *Catalysis Today* **62**, *2000*, 101–114

Figure captions

Figure 1. (a) Schematic representation of the microreactor used in this study. On the top electrode of *p*+-type Si 15 μm high micropillars are micromachined (note that the microdevies are not drawn to scale). On the bottom electrode, which acts as an ATR-internal reflection element, 140 nm SiO_2 (orange) is grown. (b)-(d) SEM images of (b) the bottom electrode of a fractured freshly coated microreactor (the inset shows a higher magnification); (c) a coated Si wafer, and (d) a bottom electrode of coated microreactor after having been subjected to CO adsorption studies. In (d) an example of coalesced particles is outlined by the ellipse. (e)-(f) Fowler-Nordheim plots extracted from the I(V) measurements for the Pt nanoparticles coated microreactors in 10% O_2/He mixture. In (e) the E-field is directed downwards (from the top towards the bottom electrode), while in (f) the E-field is directed upwards. The dotted lines are linear fits.

Figure 2. (a) ATR-IR spectra recorded during CO adsorption without an applied E-field. The inset shows a 100x magnification of the signal from 1900 to 1600 cm^{-1} after correction for water absorption, by subtraction of the last spectrum (with the water signal) of a completed adsorption/oxidation cycle. (b) ATR-IR spectra recorded at 210 min during CO adsorption pre-treatment cycles.

Figure 3. Integrated intensities of the CO_L (a-b), CO_B (c-d) and CO_{MB} (e-f) absorption bands in subsequent adsorption cycles (Sequence: 0 V, -5 V, -15 V, -25 V (in (a), (c) and (e), field downwards), 0 V(1), 0 V(2), 5 V, 15 V, 25 V(in (b), (d) and (f), field upwards)). The legend in (a) is also valid for (c) and (e), the legend in (b) for (d) and (f). Note: (a) Integrated intensities of the CO_L IR bands without applied E-field (i.e. V = 0) prior to V = -15 and V = -25 (0V(-15) & 0V(-25)).

Figure 4. ATR-IR CO absorption spectra after 200 min. exposure to CO of the reference measurements (i.e. measurements without E-field, V = 0) performed within two CO adsorption cycles in which an E-field was applied.

Figure 5. ATR-IR CO_B and CO_{MB} absorption spectra during the application of a negative potentials in (a) at V = -5, -10, -15, -25 and during the application of a positive potentials in (b) at V = 5, 10, 15, 25. The plotted spectra are time averaged from t = 150-155 min, close to the end of CO adsorption step.

Figure 6. CO_L/CO_B and CO_L/CO_{MB} ratios as a function of the applied potential. This calculation based on the averaged results in **Figure 3**. The ratios averaged after ~80 minutes.

Figure 1

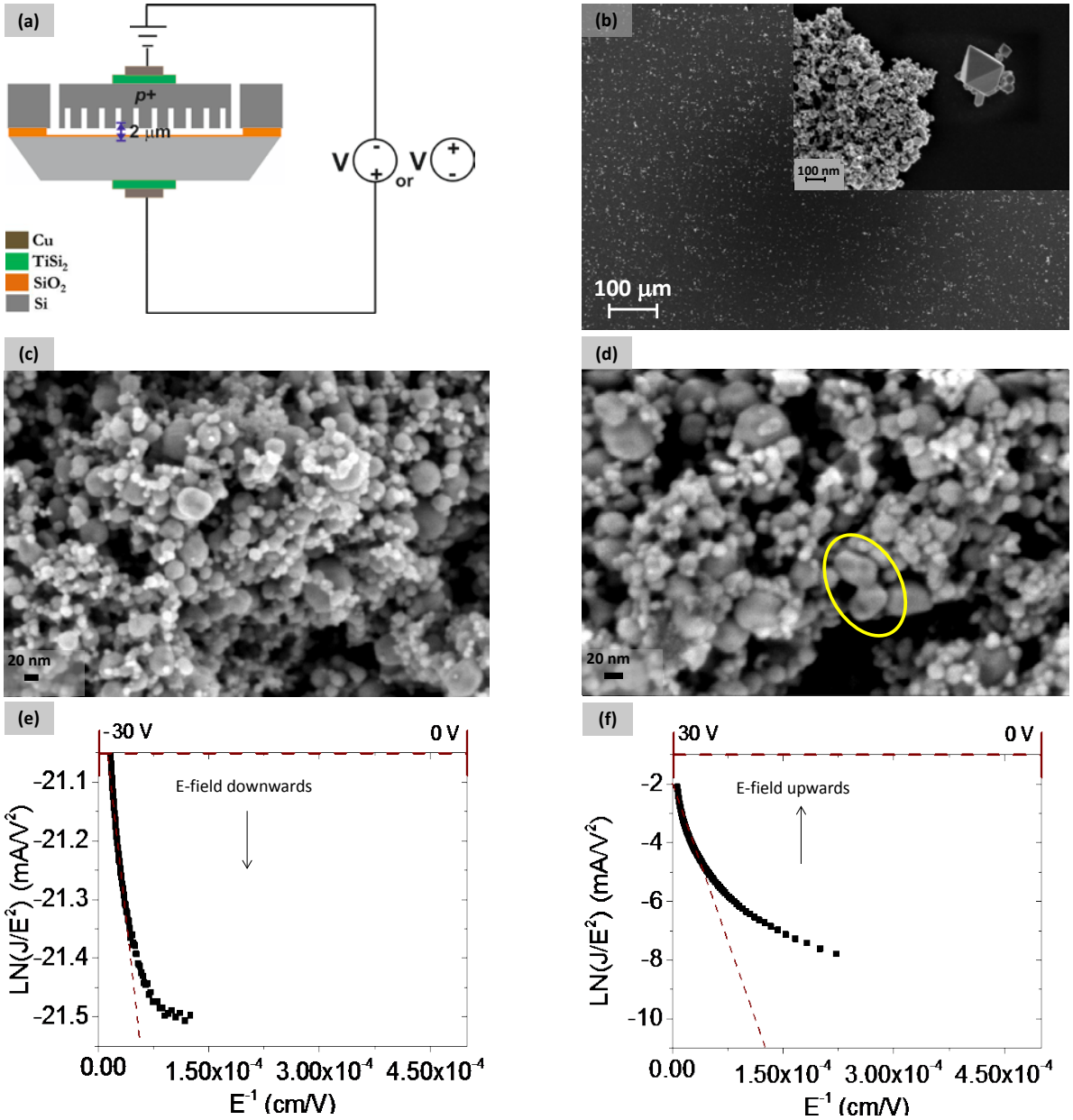
(a)
p+
2 μm
Cu
TiSi2
SiO2
Si
V
or
V
(b)
100 nm
100 μm
(c)
20 nm
(d)
20 nm
(e)
-30 V
0 V
E-field downwards
LN(J/E2) (mA/V2)
-21.1
-21.2
-21.3
-21.4
-21.5
0.00
1.50x10-4
3.00x10-4
4.50x10-4
E-1 (cm/V)
(f)
30 V
0 V
E-field upwards
LN(J/E2) (mA/V2)
-2
-4
-6
-8
-10
0.00
1.50x10-4
3.00x10-4
4.50x10-4
E-1 (cm/V)

Figure 2

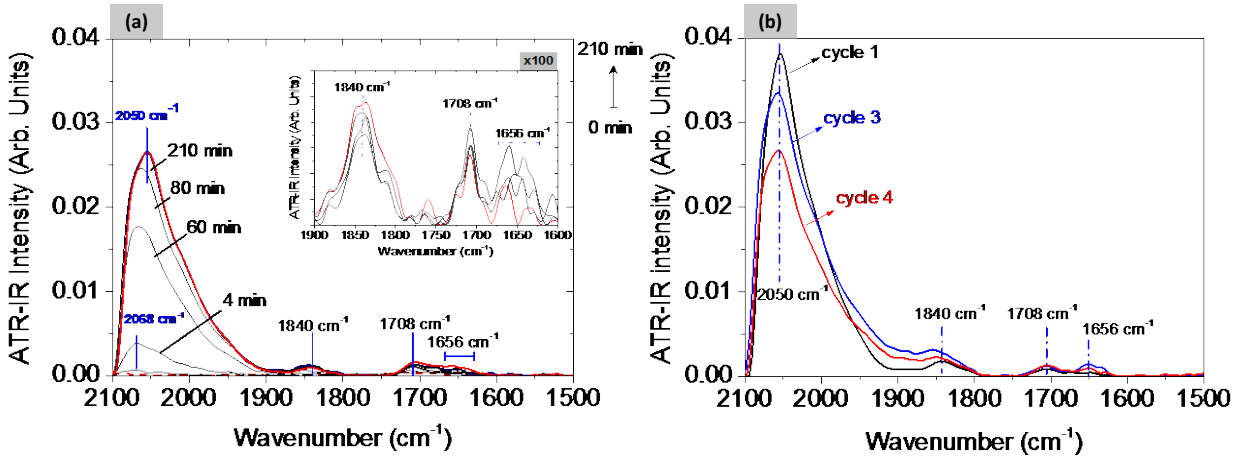
(a)
ATR-IR Intensity (Arb. Units)
Wavenumber (cm-1)
2050 cm-1
210 min
80 min
60 min
4 min
2068 cm-1
1840 cm-1
1708 cm-1
1656 cm-1
x100
210 min
0 min
(b)
cycle 1
cycle 3
cycle 4
2050 cm-1
1840 cm-1
1708 cm-1
1656 cm-1

Figure 3

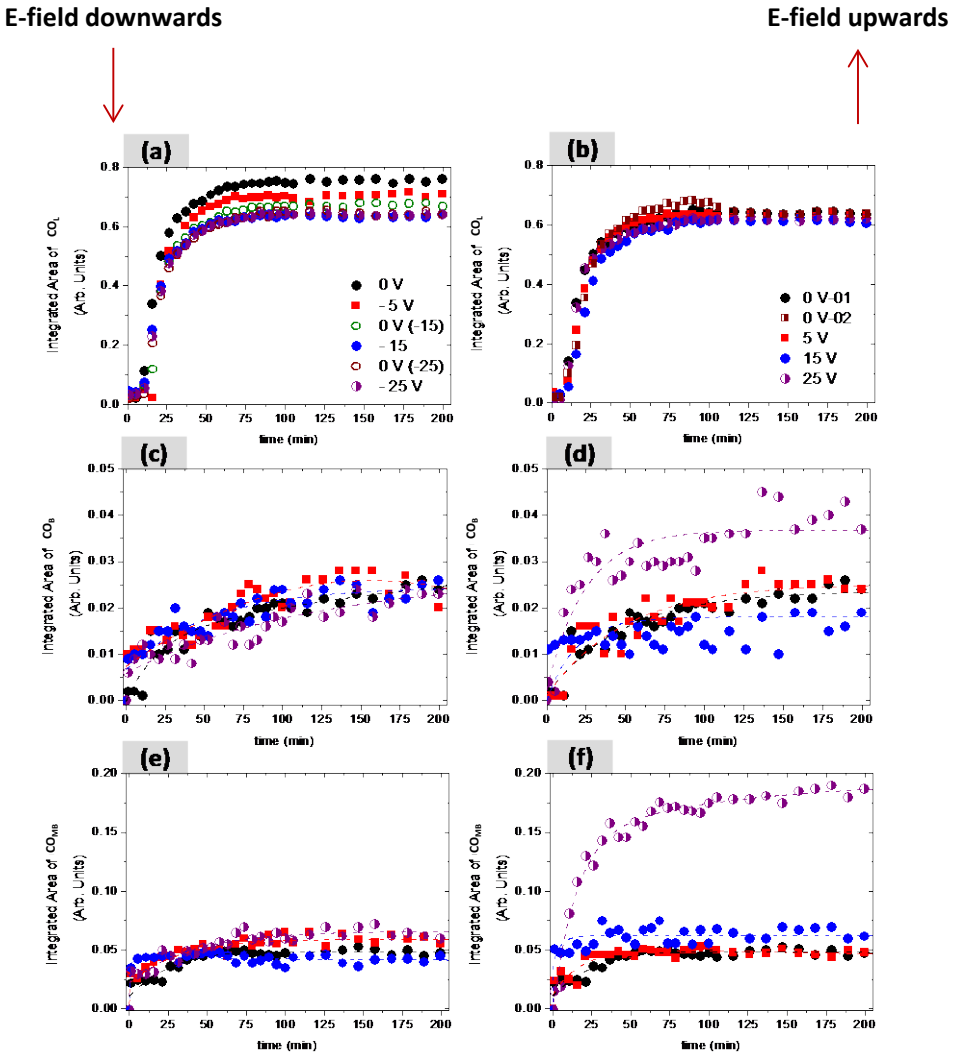
E-field downwards
E-field upwards
(a)
(b)
(c)
(d)
(e)
(f)
0 V
- 5 V
0 V (-15)
- 15
0 V (-25)
- 25 V
0 V-01
0 V-02
5 V
15 V
25 V
time (min)
Integrated Area of CO_L (Arb. Units)
Integrated Area of CO_B (Arb. Units)
Integrated Area of CO_MB (Arb. Units)

Figure 4

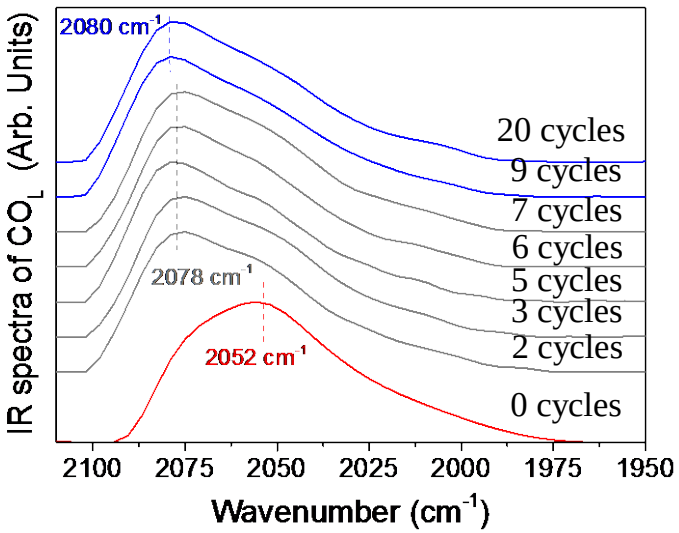
2080 cm-1
20 cycles
9 cycles
7 cycles
6 cycles
5 cycles
3 cycles
2 cycles
2078 cm-1
2052 cm-1
0 cycles
IR spectra of CO_L (Arb. Units)
2100
2075
2050
2025
2000
1975
1950
Wavenumber (cm-1)

Figure 5

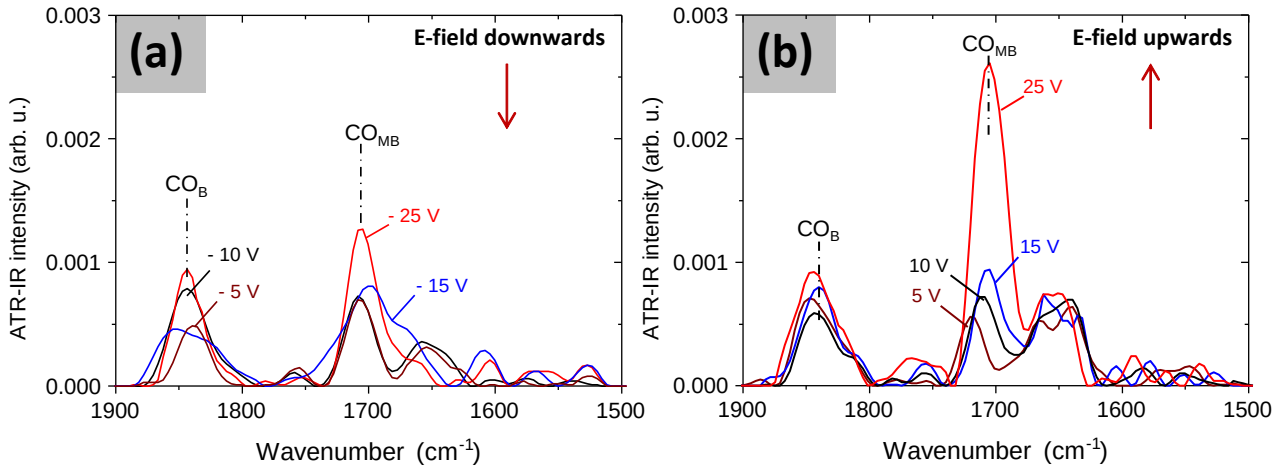
(a)
E-field downwards
CO_B
CO_MB
- 10 V
- 5 V
- 25 V
- 15 V
ATR-IR intensity (arb. u.)
Wavenumber (cm-1)
(b)
E-field upwards
CO_MB
25 V
CO_B
10 V
5 V
15 V
ATR-IR intensity (arb. u.)
Wavenumber (cm-1)

Figure 6

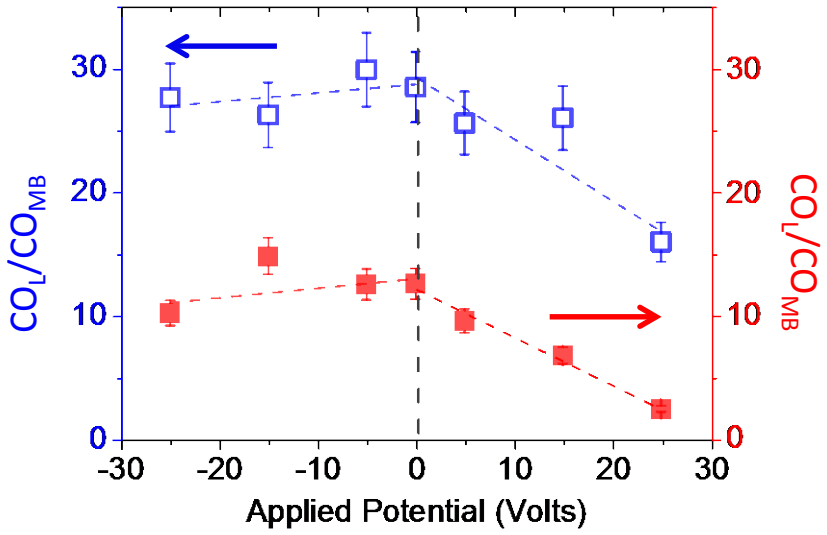
30
20
10
0
-30
-20
-10
0
10
20
30
Applied Potential (Volts)
CO_L/CO_{MB}
CO_L/CO_{MB}

Graphical Abstract

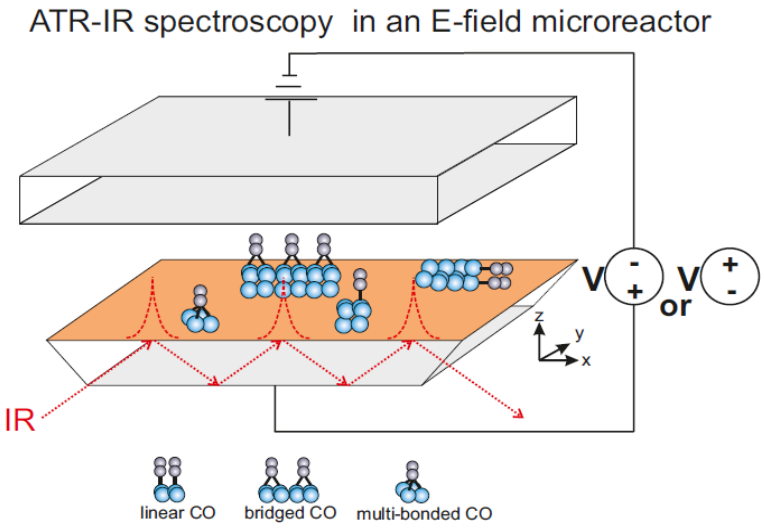

Supporting information

CO adsorption on Pt nanoparticles in low E-fields studied by ATR-IR spectroscopy in a microreactor

A. Susarrey-Arce [1, 2, 3], R. M. Tiggelaar [1], J. G. E. Gardeniers [1], A. van Houselt [2] and L. Lefferts [2]

1. Following CO adsorption experiments from **Figure 3** (see main text).